www.lpr-journal.org

# LASER & PHOTONICS REVIEWS

WILEY-VCH

WILEY ONLINE LIBRARY

Early View publication on wileyonlinelibrary.com
(issue and page numbers not yet assigned;
citable using Digital Object Identifier – DOI)

LASER & PHOTONICS REVIEWS

Laser Photonics Rev., 1–7 (2013) / **DOI** 10.1002/lpor.201200095

**Abstract** Inside of a hyperbolic medium, the principal components of the permittivity tensor have opposite signs causing the medium to exhibit a 'metallicbr' type of response to light wave sin one direction, and a 'dielectric' response in the other. Our study shows that inside hyperbolic media, *volume plasmon polaritons* (VPPs) propagate along the characteristic planes, forming distinct, directionally dependent optical responses. This is similar to the propagation of conventional surface plasmon polaritons (SPPs) along the planar interfaces separating the isotropic dielectrics and metallic slabs. Interestingly, the *plasmon polariton* propagates along the resonance cone in a *volume* of hyperbolic metamaterial crossing the interfaces of the constitutive materials. The Young's double-slit scheme is used to study the spatially-confined diffraction in a hyperbolic slab, made of many thin planar layers of a metal and dielectric, to obtain the sub-wavelength interference pattern at the output interface. Proof-of-concept systems for producing such patterns applicable to nanolithography and subwavelength probes are demonstrated.

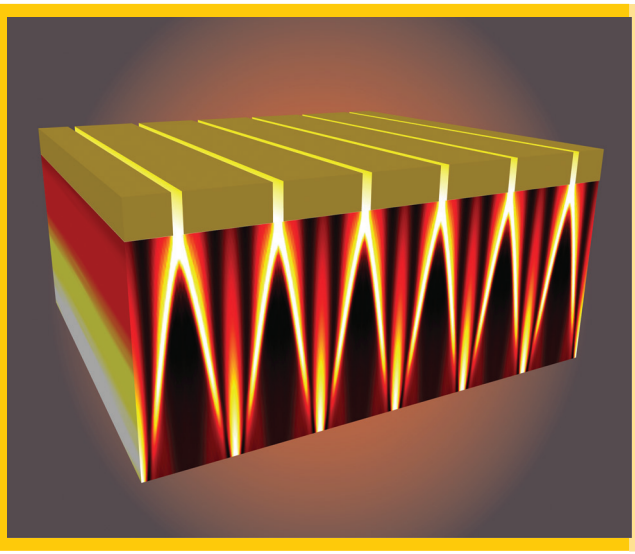

ORIGINAL PAPER

# Sub-wavelength interference pattern from volume plasmon polaritons in a hyperbolic medium

**Satoshi Ishii[1], Alexander V. Kildishev[1], Evgenii Narimanov[1], Vladimir M. Shalaev[1], and Vladimir P. Drachev[1,2,*]**

## 1. Introduction

In the 50's and 60's, many papers were published investigating electromagnetic wave propagation in a special type of anisotropic media with hyperbolic dispersion [1–5]. The permittivity components of such a medium have opposite signs, resulting in evanescent propagation of plane waves with certain direction and polarization. This research was motivated by the problem of wave propagation in a plasma of electrons and ions under the influence of a magnetic field, and in particular, radio waves in the Earth's ionosphere [3–6]. Along with the anisotropic plasmas, stratified artificial materials were studied for applications in transmission lines [1]. Recently, a more general case of indefinite metamaterial media was theoretically analyzed where both the permittivity and permeability components tensors may have opposite signs [7].

The fact that a broad spatial spectrum, including waves with a large wave-vector, can propagate in a hyperbolic media along one direction has been used to achieve extremely high spatial resolution. This property of hyperbolic materials, when used as an immersion lens, has been coined a "hyperlens" [8, 9]. Here we study a uniaxial hyperbolic metamaterial (HMM) – a lamellar metal-dielectric structure – in a regime that allows for the observation of the interference between two spatially-confined transverse-magnetic (TM) waves propagating across the metal-dielectric interfaces. Our experiments show that these highly localized waves, which we call *volume plasmon polaritons* (VPPs), propagate along the characteristic virtual interfaces separating the directions with distinct metallic and dielectric optical responses. An interference of two VPPs from the double-slit results in a sub-wavelength pattern, which is clearly demonstrated in our photolithography experiment. As a result, a route to VPP's applications to nanolithography and subwavelength light probes is demonstrated.

A significant amount of work has been done involving *surface plasmon polaritons* (SPPs) in the past few decades. Developments in SPP optics [6, 10, 11] allowed the realization of planar optical elements such as Bragg mirrors and beam splitters. These elements have been combined in various 2D SPP devices [12, 13] including interferometers, beam-splitters, mirrors, and magnifying superlenses [14]. Two dimensional double-slit experiments with SPPs on an isotropic planar metal-dielectric interface have been studied [15]. The subwavelength nature of SPPs' localization has been studied theoretically and validated experimentally

[1] Birck Nanotechnology Center and School of Electrical and Computer Engineering, Purdue University, West Lafayette, IN 47907, USA
[2] Department of Physics, University of North Texas, Denton, TX 76203, USA
*Corresponding author: e-mail: vladimir.drachev@unt.edu

with the wave-guiding of light by a subwavelength thick metal layer (see [16] and references therein).

## 2. Volume plasmon polaritons in a hyperbolic medium

The hyperbolic metamaterial design, based on alternating planar metallic and dielectric layers, supports a strong preference to the planar architecture in modern optoelectronics [17]. In our experiments, a binary metal-dielectric lamellar structure with deep subwavelength periodicity is used to effectively emulate a homogeneous hyperbolic medium [17]. The symmetry of this metamaterial medium makes it uniaxial, i.e. having $(\varepsilon_x = \varepsilon_y = \varepsilon_{x,y}) \neq \varepsilon_z$ for the principal components of its effective permittivity tensor $\varepsilon = \mathrm{diag}(\varepsilon_x, \varepsilon_y, \varepsilon_z)$, with the ordinary wave propagating along the $z$-axis. The notation $\varepsilon = \varepsilon' + \imath\varepsilon''$ is also used to denote the real and imaginary parts of those components.

In the effective medium limit, when the thickness of the individual layers is much smaller than the wavelength, the components of effective dielectric permittivity of such metamaterials are,

$$\varepsilon_{x,y} = r\varepsilon_m + (1-r)\varepsilon_d, \;\; \varepsilon_z^{-1} = r\varepsilon_m^{-1} + (1-r)\varepsilon_d^{-1}, \qquad (1)$$

where $\varepsilon_m$ and $\varepsilon_d$ are respectively the isotropic permittivities of metal and dielectric layers of thickness $\delta_m$ and $\delta_d$, and the metal volume fraction is given by $r = \delta_m/(\delta_m + \delta_d)$. Equation (1) was derived by Rytov from the exact transcendent dispersion equation for binary lamellar media [1]. Then, non-locality effects were taken into account by Agranovich *et al* [18, 19].

For a given free-space wavelength, $\lambda$ and $k = 2\pi/\lambda$, the resulting dispersion relation for normalized wavenumbers $(kk_{x,y} \to k_{x,y}, kk_z \to k_z)$,

$$k_{x,y}^2/\varepsilon_z + k_z^2/\varepsilon_{x,y} = 1, \qquad (2)$$

describes hyperbolic isofrequency wavenumber curves, provided that $\varepsilon'_{x,y}$ and $\varepsilon'_z$ have opposite signs.

Because of the optical dispersion of metal, a metal-dielectric lamellar structure can manifest metallic, epsilon-near-zero (ENZ), or dielectric properties for the adjacent wavelengths bands. Thus, Eq. (2) confirms that depending on the sign of transverse components, $\varepsilon'_{x,y}$, three different regimes for the ordinary wave propagation are possible: a metallic (transverse-negative) regime with $\varepsilon'_{x,y} < 0$ and $\varepsilon'_z > 0$, a dielectric (transverse-positive) regime with $\varepsilon'_{x,y} > 0$ and $\varepsilon'_z < 0$, and the transitional ENZ regime with $\varepsilon'_{x,y} > 0$ and $\varepsilon'_z \approx 0$. The bands of a binary silver-silica lamellar structure with $r = 1/2$ and the corresponding components of the effective permittivity tensor ($\varepsilon'_{x,y}$ and $\varepsilon'_z$) are depicted in Fig. 1 with the dielectric function of silver being taken from [20]. The dielectric and metallic HMM regimes are achieved at $328\,\mathrm{nm} < \lambda < 353\,\mathrm{nm}$ and $356\,\mathrm{nm} < \lambda$ (the blue and yellow regions in Fig. 1), respectively.

A transitional, narrow-band epsilon-near-zero (ENZ) regime occurs approximately at $353\,\mathrm{nm} < \lambda < 356\,\mathrm{nm}$,

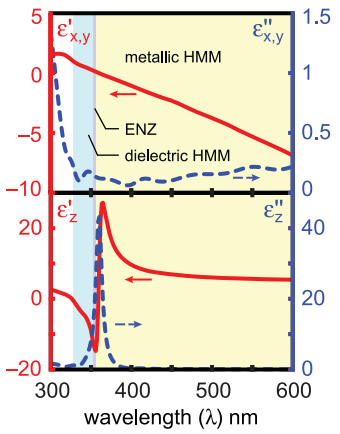


**Figure 1** (online color at: www.lpr-journal.org) Effective permittivity of a silver-silica lamellar structure having equal thicknesses. The components of the effective medium permittivity tensor, both real and imaginary parts, vs. free-space wavelength $\lambda$ (top, $\varepsilon'_{x,y}$, $\varepsilon''_{x,y}$; bottom, $\varepsilon'_z$, $\varepsilon''_z$).

where $\varepsilon'_{x,y} \approx 0$ (the narrow grey region in Fig. 1). In summary, for binary metal-dielectric lamellar structures, a metallic HMM regime is typical for the broad spectral range across the visible, the dielectric HMM regime is confined within a relatively narrow band in the ultra-violet range, while the epsilon near zero (ENZ) regime occurs in a resonant narrow band between the metallic and dielectric bands. Dielectric HMMs (with a few elemental material combinations) have been used for far-field sub-wavelength imaging [8, 9, 14, 21], which differs from the ENZ multilayer structure suggested in [22], and have been recently realized in [23, 24] for near-field imaging.

The field distribution of an electric dipole inside a uniaxial material is expressed by scaling the dielectric space [4, 25] as we will explain in detail below. In a two dimensional x-z space, for a line of dipolar sources ($\mathbf{p} = \hat{\mathbf{x}}p$) continuously distributed along $y$-axis, the $H$-field in a medium is $\mathbf{H} = \hat{\mathbf{y}}h$. We take the $H$-field pattern in vacuum, $h_0(x, z)$, and the corresponding exact $H$-field patterns $h(x, z)$, for all three regimes of the HMM, which we presented in Fig. 1.

In the wavelength-normalized free 3D-space, $kx \to x$, $ky \to y$, $kz \to z$, the TM $H$-field is defined as,

$$h_0(x, z) = -\frac{1}{4}pck^2 H_1^{(1)}(\rho)z/\rho, \qquad (3)$$

where $c$ is speed of light in free-space, $H_1^{(1)}$ is the Hankel function of the first kind and first order, $\rho = \sqrt{x^2 + z^2}$, with $z = \rho\cos\theta$, and $x = \rho\sin\theta$. Hence, the singular shadow region is aligned with the $x$-axis ($z = 0$) as depicted in Fig. 2(a). Note that the free space tangential $E$-field ($\mathbf{E} = \hat{\theta}e_0$) is $e_0(x, y) = (ze_{0,x} - xe_{0,z})/\rho$.

For the uniaxial HMM we directly use the 'Clemmow's scaling prescriptions' [4] to transform $h_0(x, z)$ into $h(x, z)$ and, $e_0(x, z)$ into $e(x, z)$ [4], we arrive at, $h(x, z) = n_z n_{x,y} h_0(n_{x,y}x, n_z z)$ and $e(x, y) =$

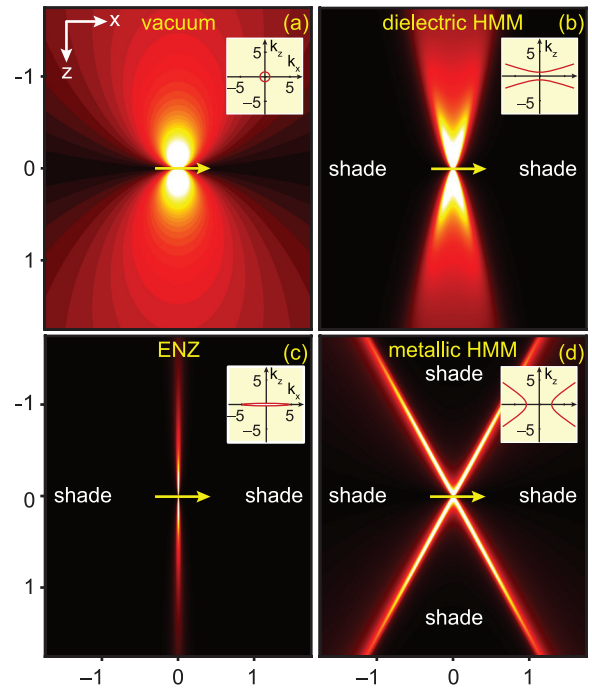


**Figure 2** (online color at: www.lpr-journal.org) Pseudo-color map of the H-field generated by an elementary electric (dipole) source. The source is an infinite line of coherent in-phase dipoles uniformly distributed along the *y*-axis (out of plane). The dipoles are aligned with the *x*-axis and generate the single *y*-component of the magnetic field. The generated H-fields are shown in the normalized space: (a) vacuum; (b) dielectric HMM at 340 nm with $\varepsilon_{x,y}$=0.57 + $\iota$0.13, $\varepsilon_z = -4.22 + \iota 2.03$; (c) ENZ at 359.4 nm with $\varepsilon_{x,y} = 0.005 + \iota 0.123$, $\varepsilon_z = 2.82 + \iota 43.3$; (d) metallic HMM at 465 nm with $\varepsilon_{x,y} = -2.78 + \iota 0.13$, $\varepsilon_z = 6.31 + \iota 0.09$. Yellow insets in (a)–(d) show the isofrequency curves for the normalized wavenumbers calculated for each material case using Eq. (2).

$n_{x,y} n_z n_\theta^{-1} e_0(n_{x,y}x, n_z y)$, where $n_{x,y} = \sqrt{\varepsilon_z}$, $n_z = \sqrt{\varepsilon_{x,y}}$, and $n_\theta = \sqrt{\varepsilon_z \sin^2\theta + \varepsilon_{x,y}\cos^2\theta}$.

As a result, for each HMM regime, the shadow and illumination regions become very different as depicted in Fig. 2(b)–(d). The tangential far-field, $\mathbf{E}(x, y) = \hat{\theta} e(x, y)$, $\rho \gg 1$, in free space is $e_0(x, z) = \eta_0 h_0(x, z)$, where $\eta_0 = \sqrt{\mu_0/\varepsilon_0}$ is the vacuum impedance. As expected, by using the *H*-field, $h(x, z)$, and the directional impedance, $\eta_\theta = n_\theta^{-1}$the far-*E*-field can be defined as $e(x, y) = \eta_0\eta_\theta h(x, z)$. Hence, we can obtain the radial component the Poynting vector from,

$$s(\rho,\theta) = \frac{1}{2}\mathrm{Re}(e\bar{h}) = \frac{1}{2}\eta_0 \mathrm{Re}(\eta_\theta)|\varepsilon_z\varepsilon_{x,y}||h_0(n_{x,y}\rho\sin\theta, n_z\rho\cos\theta)|^2. \quad (4)$$

An approximation that is commonly made for $\rho \gg 1$ is that only the lowest-power term of $\rho$ in $h_0(x, z)$ needs to be considered. Thus, for $\rho \gg 1$, the approximate free-space *H*-field is given by $h_0(x, z) \approx \frac{1+\iota 1}{4\sqrt{\pi\rho}} ck^2 e^{\iota\rho} z/\rho$. In the cylindrical coordinates, the far-field inside the HMM yields, $h(\rho, \theta) \approx \frac{1+\iota 1}{4\sqrt{\pi\rho}} ck^2 n_z^2 n_{x,y} n_\theta^{-\frac{3}{2}} e^{\iota n_\theta \rho}\cos\theta$, and Eq. (4) gives the following approximation ($\rho \gg 1$):

$$s(\rho,\theta) \approx \frac{\eta_0 \left|n_z^2 n_{x,y}\right|^2}{16\pi |n_\theta|^5 \rho} c^2 k^4 \mathrm{Re}(n_\theta) e^{-2n''_\theta \rho}\cos^2\theta. \quad (5)$$

To illustrate the radiation patterns specific to the unique anisotropy of the HMM, an electric dipole radiation in a homogenized isotropic medium of the silver-silica lamellar structure is shown in Fig. 2. In this figure, we compare an *H*-field map generated by an infinite line of electric dipolar sources $\mathbf{p} = \hat{\mathbf{x}} p$ in vacuum (Fig. 2(a)) with the corresponding field maps in given HMM regimes (Fig. 2(b)–(d)) where the effective permittivities are taken from Fig. 1.

The ENZ regime gives low divergence due to the highly anisotropic elliptical dispersion (see, Fig 2(c)), while dielectric HMM dispersion may result in a similar directional propagation along the *z*-axis (normal to the surface of metal-dielectric layers), as shown in Fig. 2(b). These types of propagation were studied in experiments on hyperlenses [14,21]. In this case, light propagates along the optical axis of the anisotropic structure.

Consider a slab of hyperbolic uniaxial medium with optical axis in the z-direction and the displacement vector D lying in the principal plane containing both optic axis and wave vector k. Component of electric field directed along D is given by $E_D = \mathbf{E}\cdot\mathbf{D}/|\mathbf{D}| = |\mathbf{D}|/\varepsilon(\varphi)$, where

$$\frac{1}{\varepsilon(\varphi)} = \frac{\sin^2\varphi}{\varepsilon_e} + \frac{\cos^2\varphi}{\varepsilon_o} \quad (6)$$

here $\varepsilon_o = \varepsilon_{x,y}$, $\varepsilon_e = \varepsilon_z$ and $\varphi$ is the angle between the wave vector and optical axis. The wave vector refraction at the crystal-isotropic medium interface formally obeys the Snell's law. The critical angle $\varphi_c$ for the wavevector can be found from the angular dependence of the effective permittivity, $\varepsilon(\varphi)$, calculated from Eq. (6) at $\mathrm{Re}(\varepsilon(\varphi)) = 0$ as shown in Fig. 3(a) at 456 nm. As in turn the angle $\theta$ between the ray and optical axis depend on $\varphi$ as $\tan\theta = (\varepsilon_o/\varepsilon_e)\tan\varphi$, as depicted in Fig. 3(b). Then, the critical angle $\theta_c$ for the resonance cone can be found from $\theta_c = \tan^{-1}(\mathrm{Re}(\varepsilon_o/\varepsilon_e)\tan\varphi_c)$.

The table in Fig. 3(c) compares the critical angles ($\theta_c$) obtained either directly at max $|s(\rho, \theta)|$, with the Poynting vector $s(\rho, \theta)$ being defined by Eq. (4), or indirectly from the resonance condition $\mathrm{Re}\,\varepsilon(\varphi_c) = 0$. The differences between the two methods do not exceed more than one degree in the visible range, as illustrated in Fig. 3(c). The angular dependences of the normalized Poynting vector amplitudes, calculated from Eq. (4) as well as from Eq. (5), are shown in Fig. 3(d). Figure 3(d) clearly shows the wedge-confined energy flow at the critical angle $\theta_c \approx -32$ deg. So the *plasmon polariton* in this case propagates along the resonance cone in a *volume* of hyperbolic metamaterial.

Note that by confining the propagating modes inside the metallic medium along the resonance cone (Fig. 2(d)),

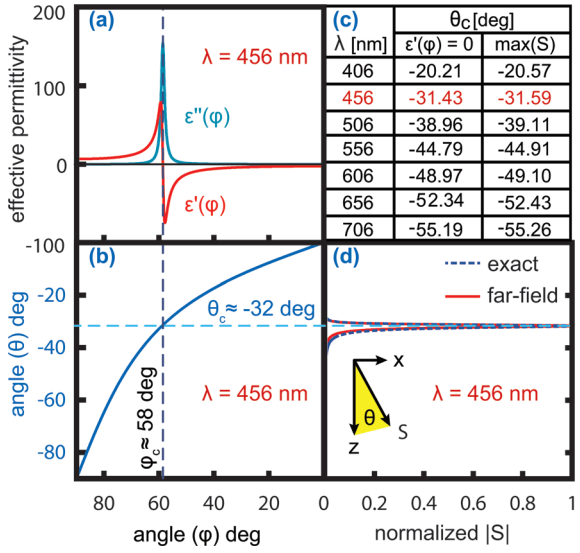


**Figure 3** (online color at: www.lpr-journal.org) Angular dependence of VPPs for a silver-silica lamellar structure. (a) the angular dependence of the effective permittivity (red, $\varepsilon'(\varphi)$; blue, $\varepsilon''(\varphi)$) calculated from Eq. (6); (b) the critical angle of the resonance cone $\theta_c$ obtained using the dependence $\tan\theta = (\varepsilon_o/\varepsilon_e)\tan\varphi$ shown as a solid-red line; (c) wavelength dependence of the VPP angles: comparison of the critical angles ($\theta_c$) obtained either through $\varphi_c$ from the resonance condition $\varepsilon'(\varphi_c) = 0$ for Eq. (6) and $\theta_c = \tan^{-1}[\mathrm{Re}(\varepsilon_o/\varepsilon_e)\tan\varphi_c]$, or directly from max $|s(\rho,\theta)|$. (d) normalized Poynting vector amplitude calculated from the exact formula (Eq. (4) and the far-field approximation (Eq. (5) plotted against angle ($\theta$).

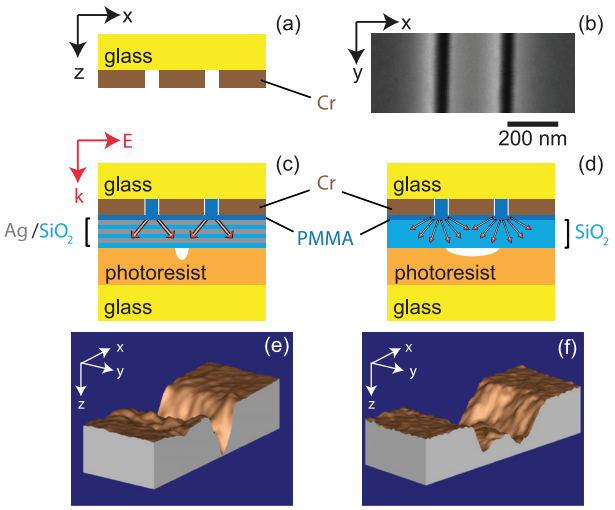


**Figure 4** (online color at: www.lpr-journal.org) Schematic diagram (a) and a SEM image (b) of the double slit milled in a chromium film. (c) Schematic diagram of the double slit with a silver-silica lamellar HMM slab in contact with a photoresist layer. (d) Schematic diagram of double slit with a reference silica slab in contact with a photoresist layer. Incident and diffracted fields are shown in red. AFM images after develop for the silver-silica lamellar HMM sample (e) and the silica layer sample (f). The dimensions of the images in x axis are 600 nm and 1000 nm for (e) and (f), respectively. The dimensions of the images for (e) and (f) in x and y directions are 1500 nm and 600 nm, respectively.

two-beam interference can be accomplished. Thus, in contrast to the imaging devices built on ENZ materials and dielectric HMMs [8, 9, 26–28], optical devices exploiting wedge-confined diffraction in the metallic hyperbolic media may offer lucrative applications for photo-lithography and light response probing.

Several numerical studies have shown that it is possible to obtain an interference peak much smaller than the free-space wavelength [29–33]. There are however many aspects of light-matter interaction in such hyperbolic metamaterials to be clarified for experimental realization. These include the essentially nonlocal response of the free electrons [34] (defined by the carrier mean-free path) and the defects at the layer boundaries which can lead to strong scattering into the high-$k$ modes of the hyperbolic media. These issues are especially crucial in the case of the metallic range of hyperbolic media supporting VPPs (see isofrequency curve in Fig. 2(d)).

## 3. Experimental demonstration of sub-wavelength interference in a hyperbolic medium

Next, we experimentally demonstrate that the metallic HMMs support propagation of the VPPs along the wedge surface defined by the condition of crossing zero epsilon ($\varepsilon'(\varphi_c) = 0$, i.e. the boundary of the evanescent wave). An interference of two volume waves from individual double-slits results in a sub-wavelength pattern, which is clearly demonstrated in our photolithography experiment. We see that the interfering waves go through the hyperbolic multilayer metamaterial and hit the photoresist layer. Different power-to-time product of the exposure show similar patterns at different depths. Due to localized propagations of the VPPs, a relatively thin structure supports the interference of the two beams, simplifying its fabrication and integration into a potential planar photonic device. Thus, the operation principles and design of our focusing device are different from imaging or transformation optics devices such as the designs of cylindrical hyperlens or planar hyperlens requiring curved layers [8, 9, 26–28].

The fabrication process began by depositing a 50-nm chromium film on a glass substrate using an electron-beam evaporator. The double slit design was then milled into the chromium film using a focused ion beam (FIB) (FEI, Nova 200). A schematic diagram and a scanning electron microscope (SEM) image of the double slit are shown in Fig. 4(a) and (b), respectively. The separation of the two slits is 270 nm, and the width of each slit is 50 nm. In order to fill the slits, we spin-coated diluted PMMA on the chromium film. The PMMA solution was prepared by diluting 950PMMA A4 (MicroChem Corp.) with Anisole in a one to four volume ratio. This gives a final film thickness of 18 nm after spin coating at 3000 rpm for 40 seconds and a soft-bake

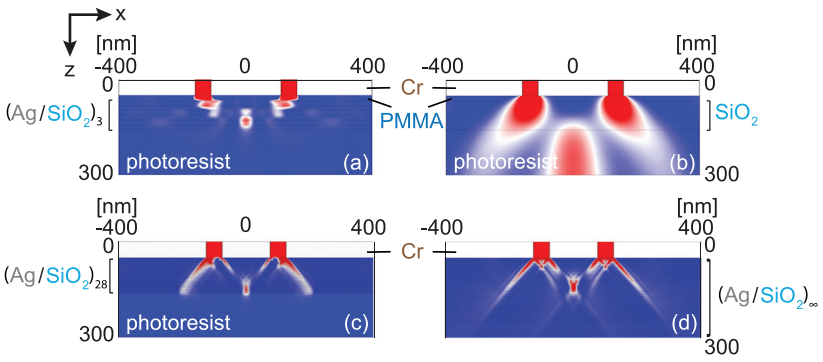


**Figure 5** (online color at: www.lpr-journal.org) (a) and (b): Simulated irradiances through the double slit at 465 nm in the silver-silica lamellar HMM slab with 15-nm thick layers of silver and silica (a) and in the single layer of silica (b). These structures correspond to the experimentally fabricated samples. (c) and (d): Same as (a) and (b), but with 2-nm thick layers of silver and silica: (c) an HMM with 28 pairs of layers; (d) semi-infinite HMM slab. The color scales in (a), (c) and (d) are normalized to each diffraction peak irradiance and the color scale in (b) is same as (a).

at 185°C for 5 min on a hotplate. On top of the PMMA layer, we deposited three pairs of alternating silver and silica layers for a total of six 15-nm-thick layers. To have a smooth and continuous silver film, 1-nm-thick germanium layers were deposited before each of the silver layers [35]. Hence, the final structure looks like the images shown in Fig. 4(c) and the total thickness of the multilayer structure including the PMMA layer was 111 nm. From spectroscopic ellipsometry measurements, the permittivities of the silver and silica layer were found to be $7.82 + \imath 0.45$ and 2.1, respectively at 465 nm. The imaginary part of the permittivity of silver was 1.7 times larger than the value given in [20] due to the film thickness, which is less than the electron mean free path [36] and unavoidable grain structures [37]. We also prepared a control sample consisting of a single 110-nm-thick layer of silica instead of the alternating metal-dielectric layers (see Fig. 4(d)).

To detect the diffraction pattern, we exposed positive photoresist (AZ Electronic Materials, AZ 1518) films. The photoresist was spin-coated on a glass substrate. The light source used for exposing the photoresist was a linearly polarized 3 mW Ar/Kr CW laser (Melles Griot, 43 series) operating at 465 nm. Since the transmittance of the silica layer sample is higher than the transmittance of the HMM sample, the laser power was decreased by 20% when exposing the silica layer sample to keep the exposure time the same as the HMM sample. When exposing the sample, the photoresist was brought into contact with the sample, and the sample was illuminated from the Cr film side in TM polarization as shown in Fig. 4(c) and (d). Light coming out from subwavelength slits can be treated as point sources. The arrows in Fig. 4(c) and (d) schematically show the light propagation in each structure.

After exposure, the photoresist was developed with AZ developer (AZ Electronic Materials) for one minute. The dip created by the photolithography process was scanned by an atomic force microscope (AFM, Veeco Dimension 3100) with a high-aspect ratio tip (Veeco Nanoprobe Tip TESP-HAR) to detect narrow features. The root-mean-square (RMS) roughness of our sample, in addition to the photoresist, was below 1.5 nm. Examples of the AFM scans for the silver-silica lamellar HMM sample and the silica layer sample are shown in Fig. 4(e) and (f), respectively. The dip created by the HMM sample is much narrower compared the dip created by the silica layer sample.

To verify our experimental results on the interference of VPP waves inside the HMM, and optimize the performance of the double-slit/HMM device, we have conducted full-wave simulations using a commercial finite-element software (COMSOL Multiphysics), with all dimensions taken from the fabricated samples. The permittivities of the materials are extracted from spectroscopic ellipsometry measurements. The computational domain was truncated by the scattering boundary condition, and a 465-nm TM-polarized plane wave (electric field is across the slits, see Fig. 4(c)) was incident from the top boundary. The control structure which has a single layer of silica instead of the lamellar structure was also simulated. The irradiance of the transmitted light for the silver-silica lamellar HMM and the silica reference slabs are shown in Fig. 5(a) and (b), respectively. While the silica slab creates a diffraction-limited pattern, the HMM directs the diffracted light into a subwavelength spot at the HMM-substrate interface due to the directional propagation of high-$k$ waves from the slits. Note that inside HMM pattern light is still "diffraction limited" but this limit is much less for the hyperbolic media as compared to free space.

Even for the HMM described with a relatively small number of the metal-dielectric layers, the effective permittivity is still hyperbolic [1,38]. Nonetheless, the limitations of the EMT approximation become significant [1, 39, 40]. One of the indications of that is the beam walk-off parallel to the interfaces as seen in the simulations (Fig. 5(a)). Some changes in the results should be expected, once the period of the HMM structure is decreased, leaving the effective parameters formally the same. The computed hypothetical HMM structure consists of 28 pairs of silver and silica layers, each with a 2-nm thickness. The total thickness would then be 112 nm, which is approximately same as the experiment. The distance between the two slits was set to 200 nm to maximize the irradiance at the center as shown in Fig. 5(c). Since this structure has a smaller period, its performance becomes closer to the homogeneous effective medium. Compared to Fig. 5(a), we see more distinct beaming in Fig. 5(c). In terms of the beam propagation angle, the angles in Fig. 5(a) and (c) are 51 and 40 deg, respectively. Thus, the structure in Fig. 5(c) gives the angle which is closer to that obtained from the VPP condition ($|\theta_c| \approx 33$ deg at 465 nm). More importantly, the pattern size is significantly decreased as shown below in Fig. 5(c).

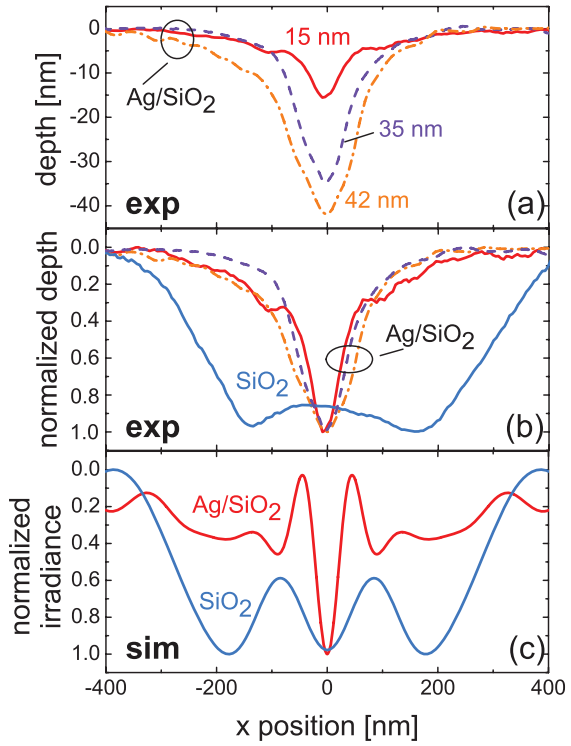


**Figure 6** (online color at: www.lpr-journal.org) (a) Depth profiles from the AFM scans for the silver-silica lamellar HMM sample having three different depths depending on exposure conditions. (b) Normalized depth profiles of the HMM sample shown in (a) and the silica layer sample. The actual depth for the silica layer sample is 112 nm. (c) Simulated irradiances at the slab-substrate interface for the lamellar HMM slab and the uniform slab of silica.

We also plot a semi-infinite slab of alternating 2-nm thick silver/silica layers (Fig. 5(d)). The FWHM is about the same as in Fig. 5(c) which means that back reflection at the interface does not affect the pattern size. Note that before the experiments, the initial EMT-based estimates have been followed by full-wave modeling to optimize the center peak intensity by varying the distance between the slits.

Fig. 6(a) shows the AFM scans averaged along the slits for the silver-silica lamellar HMM sample deposed for 8 to 10 minutes. When the pattern depth in photoresist is 15 nm, the full-width-at-half-maximum (FWHM) is 83 nm. Longer exposure time resulted in a deeper profile and wider FWHM. Thus, for the writing depths of 35 nm and 42 nm the FWHMs are 105 nm and 135 nm, respectively. Our results clearly indicate that planar metal-dielectric lamellar structures have the capability to form the diffracted light from the slits into a subwavelength interference spot. In Fig. 6(b), we show the normalized AFM scans presented in Fig. 6(a) as well as the silica layer sample. As the penetration depth (exposure time) increases, the contrast becomes better while the FWHM becomes larger. If the experimental profile was extrapolated to an even smaller depth, the side peaks would grow and the central peak would become narrower, approaching the simulated irradiance just near the resist's surface. Fig. 6(c) depicts the irradiances at the interfaces and the substrate obtained from the simulations

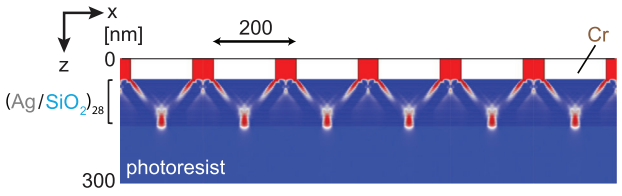


**Figure 7** (online color at: www.lpr-journal.org) Numerically simulated grating nanolithography pattern with metallic hyperbolic medium.

shown in Fig. 5. The FWHM of the central peaks of the HMM structure and the single layer are 45 nm and 514 nm, respectively. Thus, the results of the numerical simulation results agree with our experimental results. Our separate simulations (with the photoresist being replaced with air) show that the minimum FWHM does not depend on the substrate index. When comparing the experimental results with the simulations, it is important to keep in mind that the tightest spot is at the interface of the top layer (silica) and the resist for the HMM sample. As the distance from the interface increases, the peak-to-background ratio becomes worse. This happens because the photoresist is not a hyperbolic medium, and therefore the waves entering the photoresist from the multilayers diverge within a few tens of nanometers. Since the depth of the surface profile is 15 nm even for the shallowest result, it is natural that the FWHM of the experimentally measured dip is wider than that from the simulation results of Fig. 6(c). The overall picture becomes closer to the simulated results if the depth of the dip is shallower. The simulations for the 28 layer structure show potential to improve the resolution. Indeed the FWHM of the interference peak for this short period structure is about 22 nm. Reducing the metallic losses could further improve the resolution as discussed in [29]. However, to reach this resolution the photoresist quality should be improved. Commercially available photoresists at the tested wavelength have grains of at least 60 nm [41]. However, PMMA could be grafted with azobenzene dye for better resolution down to 30 nm [42]. Our results can be easily extended to the grating nanolithography as it is shown in Fig. 7.

## 4. Summary

To summarize, we have experimentally shown that diffracted light propagates inside a hyperbolic material made of a planar silver-silica lamellar structure along the resonance cone boundary between the directions with $\mathrm{Re}\,\varepsilon(\varphi_c) > 0$ and $\mathrm{Re}\,\varepsilon(\varphi_c) < 0$. Such propagation across the real metal-dielectric interfaces is a characteristic feature of the volume plasmon-polaritons. The interference of VPPs from a double-slit creates a sub-wavelength interference pattern, which is six times smaller than the free space wavelength at 465 nm. This is in sharp contrast to the double-slit experiment in silica, which results in a diffraction-limited pattern. The hyperbolic material properties tend to be closer to the target effective parameters as

the layering-period is decreased, providing potential pattern sizes of 22 nm. Such unique subwavelength interference patterns offered by hyperbolic metamaterials allow for a range of applications in nanophotonics – from photolithography demonstrated in our work, to a sub-wavelength optical probe for sensing. Planar structures are preferred due to their ease of fabrication and integration into planar photonic devices and conventional optical systems.

**Acknowledgements.** The authors would like to thank M. D. Thoreson for his kind assistance with manuscript preparation. This work was supported in part by ONR MURI grant N00014-010942, ARO MURI Awards 50342-PH-MUR, and NSF-DMR 1120923. AVK and VPD want also to thank a partial support by AFRL Materials and Manufacturing Directorate – Applied Metamaterials Program. SI was supported by the JSPS Postdoctoral Fellowships for Research Abroad.

**Received:** 19 October 2012, **Revised:** 30 December 2012, **Accepted:** 2 January 2013

**Published online:** 28 January 2013

**Key words:** Metamaterials, hyperbolic dispersion, diffraction, metal-dielectric lamellar structures.

## References

[1] S. M. Rytov, Sov. Phys. JETP **2**, 466–475 (1956).
[2] F. V. Bunkin, Sov. Phys. JETP **5**, 277–283 (1957).
[3] K. G. Budden, *Radio waves in the ionosphere* (Cambridge University Press, 1961).
[4] P. Clemmow, Proc. IEE **110**, 101–106 (1963).
[5] N. Marcuvitz and L. B. Felsen, Radiation and scattering of waves (Wiley-IEEE Press, 1973).
[6] R. H. Ritchie, Phys. Rev. **106**, 874–881 (1957).
[7] D. R. Smith and D. Schurig, Phys. Rev. Lett. **90**, 077405 (2003).
[8] Z. Jacob, L. V. Alekseyev, and E. Narimanov, Opt. Express **14**, 8247–8256 (2006).
[9] A. Salandrino and N. Engheta, Phys. Rev. B **74**, 075103 (2006).
[10] H. Raether, Surface Plasmons (Springer-Verlag Berlin, 1988).
[11] B. Hecht, H. Bielefeldt, L. Novotny, Y. Inouye, and D. Pohl, Phys. Rev. Lett. **77**, 1889–1892 (1996).
[12] S. I. Bozhevolnyi and F. A. Pudonin, Phys. Rev. Lett. **78**, 2823–2826 (1997).
[13] H. Ditlbacher, J. Krenn, G. Schider, A. Leitner, and F. Aussenegg, Appl. Phys. Lett. **81**, 1762 (2002).
[14] I. I. Smolyaninov, Y. J. Hung, and C. C. Davis, Science **315**, 1699 (2007).
[15] R. Zia and M. L. Brongersma, Nat. Nanotechnol. **2**, 426–429 (2007).
[16] J. Burke, G. Stegeman, and T. Tamir, Phys. Rev. B **33**, 5186 (1986).
[17] A. J. Hoffman, L. Alekseyev, S. S. Howard, K. J. Franz, D. Wasserman, V. A. Podolskiy, E. E. Narimanov, D. L. Sivco, and C. Gmachl, Nat. Mater. **6**, 946–950 (2007).
[18] V. Agranovich, Solid State Commun. **78**, 747–750 (1991).
[19] V. Agranovich and V. Kravtsov, Solid State Commun. **55**, 85–90 (1985).
[20] P. B. Johnson and R. Christy, Phys. Rev. B **6**, 4370 (1972).
[21] Z. Liu, H. Lee, Y. Xiong, C. Sun, and X. Zhang, Science **315**, 1686 (2007).
[22] S. A. Ramakrishna, J. Pendry, M. Wiltshire, and W. Stewart, J. Mod. Opt. **50**, 1419–1430 (2003).
[23] D. O. S. Melville and R. J. Blaikie, J. Opt. Soc. Am. B **23**, 461–467 (2006).
[24] G. Li, J. Li, H. Tam, C. Chan, and K. Cheah, J. Nanosci. Nanotechnol. **11**, 10725–10728 (2011).
[25] A. S. Potemkin, A. N. Poddubny, P. A. Belov, and Y. S. Kivshar, Phys. Rev. A **86**, 023848 (2012).
[26] A. V. Kildishev and V. M. Shalaev, Opt. Lett. **33**, 43–45 (2008).
[27] W. Wang, H. Xing, L. Fang, Y. Liu, J. Ma, L. Lin, C. Wang, and X. Luo, Opt. Express **16**, 21142–21148 (2008).
[28] Y. Xiong, Z. Liu, and X. Zhang, Appl. Phys. Lett. **94**, 203108 (2009).
[29] S. Thongrattanasiri and V. A. Podolskiy, Opt. Lett. **34**, 890–892 (2009).
[30] L. Verslegers, P. B. Catrysse, Z. Yu, and S. Fan, Phys. Rev. Lett. **103**, 33902 (2009).
[31] G. Ren, Z. Lai, C. Wang, Q. Feng, L. Liu, K. Liu, and X. Luo, Opt. Express **18**, 18151–18157 (2010).
[32] C. Ma and Z. Liu, Appl. Phys. Lett. **96**, 183103 (2010).
[33] G. Li, J. Li, and K. W. Cheah, Appl. Opt. **50**, G27–G30 (2011).
[34] A. I. Fernández-Domínguez, A. Wiener, F. J. García-Vidal, S. A. Maier, and J. B. Pendry, Phys. Rev. Lett. **108**, 106802 (2012).
[35] W. Chen, M. D. Thoreson, S. Ishii, A. V. Kildishev, and V. M. Shalaev, Opt. Express **18**, 5124–5134 (2010).
[36] V. P. Drachev, U. K. Chettiar, A. V. Kildishev, H. K. Yuan, W. Cai, and V. M. Shalaev, Opt. Express **16**, 1186–1195 (2008).
[37] K. P. Chen, V. P. Drachev, J. D. Borneman, A. V. Kildishev, and V. M. Shalaev, Nano Lett. **10**, 916–922 (2010).
[38] J. Kim, V. P. Drachev, Z. Jacob, G. V. Naik, A. Boltasseva, E. E. Narimanov, and V. M. Shalaev, Opt. Express **70**, 8100–8116 (2012).
[39] B. Wood, J. Pendry, and D. Tsai, Phys. Rev. B **74**, 115116 (2006).
[40] X. Ni, S. Ishii, M. D. Thoreson, V. M. Shalaev, S. Han, S. Lee, and A. V. Kildishev, Opt. Express **19**, 25255–25262 (2011).
[41] D. O. S. Melville and R. J. Blaikie, Opt. Express **13**, 2127–2134 (2005).
[42] R. Bachelot, F. H'Dhili, D. Barchiesi, G. Lerondel, R. Fikri, P. Royer, N. Landraud, J. Peretti, F. Chaput, and G. Lampel, J. Appl. Phys. **94**, 2060 (2003).